PHYSICAL REVIEW C **93**, 054602 (2016)

Energy dependence of mass, charge, isotopic, and energy distributions in neutron-induced fission of ^{235}U and ^{239}Pu

H. Pasca,[1,2] A. V. Andreev,[1] G. G. Adamian,[1] N. V. Antonenko,[1,3] and Y. Kim[4]
[1]*Joint Institute for Nuclear Research, 141980 Dubna, Russia*
[2]*Babes-Bolyai University, 400084 Cluj-Napoca, Romania*
[3]*Mathematical Physics Department, Tomsk Polytechnic University, 634050 Tomsk, Russia*
[4]*Rare Isotope Science Project, Institute for Basic Science, 305-811 Daejeon, Korea*
(Received 7 July 2015; revised manuscript received 19 February 2016; published 2 May 2016)

The mass, charge, isotopic, and kinetic-energy distributions of fission fragments are studied within an improved scission-point statistical model in the reactions ^{235}U $+n$ and ^{239}Pu $+n$ at different energies of the incident neutron. The charge and mass distributions of the electromagnetic- and neutron-induced fission of ^{214,218}Ra , ^{230,232,238}U are also shown. The available experimental data are well reproduced and the energy-dependencies of the observable characteristics of fission are predicted for future experiments.

DOI: 10.1103/PhysRevC.93.054602

I. INTRODUCTION

As known, the mass (charge) distributions of the neutron-induced fission of pre-actinides are symmetric, while the fission of the nuclei U–Cf and Ac–Pa near the line of stability results in asymmetric mass (charge) distributions with two and three maxima, respectively [1,2]. For neutron-deficient actinides Ac–U, the symmetric fission mode dominates. However, in neutron-deficient ^{180}Hg the asymmetric mass distribution of fission fragments was unexpectedly observed in the recent experiment [1,3]. Despite seven decades of the experimental and theoretical research, there is still no good understanding why the transition from symmetric to asymmetric fission occurs with increasing mass or decreasing excitation energy of the fissioning nucleus. In Ref. [4], the competition between symmetric and asymmetric fission was suggested to be related to the shell effects in the deformed fissioning nucleus. With increasing energy the shell effects are washed out, leaving the nucleus with a dominant symmetric mode of fission. Note that the multimodal random neck rupture model used in Ref. [4] is rather phenomenological. One of the main ingredients of this model is the stiffness of the macroscopic potential with respect to mass asymmetry which is deduced from the widths of measured mass distributions. However, the new experimental data on the fission of ^{180}Hg show that the asymmetric mass distribution cannot be created with the weak microscopic effects in the fission fragments. The experimental nuclear-charge distributions of fission fragments of nuclei At–U with $A < 220$ do not show any clear signature of the shell effects [2]. The peak-to-valley ratio and the even-odd effect in the charge distributions in the electromagnetic-induced fission of ^{233,234}U cannot be quantitatively understood on the basis of previously measured thermal-neutron–induced data on the excitation-energy dependence of fission characteristics [2]. So, further theoretical and experimental investigations of the mass (charge) distributions and their energy dependence are required.

There is another longstanding question. At which point of the fission path are the mass (charge) and energy distributions of the fission fragments determined? There exist several versions of "saddle-point models" and "scission-point models" which put this crucial point closer either to the saddle- or to the scission-point, respectively [4–10]. There is also dynamical approach [11] where the potential-energy surface in the entire deformation range from the saddle-point to scission-point governs the final yields of the fission fragments. The detailed analysis indicates that the formation of the observed total kinetic energy- and mass-distributions of the fission fragments occurs in the region closer to the scission region rather than to the saddle point. As shown in Ref. [11], the mass-asymmetry distribution reflects the structure of the potential-energy surface in the scission region. In this region, the fissioning nucleus has well-necked-in shape and the fragments attain their individual character. With the scission-point model the experimental data on fission of actinides and pre-actinides: mass, charge, energy, and neutron multiplicity distributions are well described [6,9]. The wide range of described fission observables and effects confirms the predictive power of this model.

Although the fission product mass distributions have been essentially compiled for the fission of ^{235}U by thermal neutrons and low-energy neutrons ($E_n \leqslant 10$ MeV) [12,13], relatively little data [14–16] are available on the characteristics of mass distributions for monoenergetic-neutron-induced fission as a function of incident neutron energy $E_n > 10$ MeV. The fission-fragment-mass yields for neutron-induced fission of ^{232}Th and ^{238}U at energies 32.8, 45.3, and 59.9 MeV have been recently measured [15]. The experimental results [15] demonstrated that the probability of symmetric fission increases with incident neutron energy for both nuclei. Note that new experimental data on the bremsstrahlung-, charged-particle-, and nucleon-transfer-induced fission at the high excitation energies of the compound nucleus [10,17–20] have recently appeared.

In this paper, we study the evolution of the shape of charge and mass distributions of the fission fragments for the reactions ^{235}U(n,f) and ^{239}Pu(n,f) with increasing incident neutron energy from the thermal energy up to 55 MeV. The present work will be undertaken to explore systematically the characteristics of the mass distribution as a function of E_n at $E_n > 10$ MeV. As is well known, the thermal-neutron-induced fission products of nuclei ^{235,238}U and ^{239}Pu have the two humped charge and mass distributions. The fission observables will be described in the statistical way employing the dinuclear system (DNS) model [6,9,21] which is the improved scission-point approach. The main ingredient of our description is the sophisticated potential energy as a function of mass (charge) asymmetry, deformations of nuclei, and internuclear distance. The knowledge of the deformations of the nascent DNS fragments is crucial at the moment of scission.

This article is organized as follows: In Sec. II we present our model. The results of calculations are discussed in Sec. III. A brief summary is given in Sec. IV.

II. MODEL

The statistical scission-point model relies on the assumption that the statistical equilibrium is established at scission and the observable characteristics of fission processes are formed near the prescission configurations of the fissioning nucleus. The DNS model is well suited for describing the scission configuration, which consists of two well-defined fission fragments in contact. The fissioning nucleus at the scission point is modeled by two nearly touching coaxial ellipsoids—fragments of the DNS with mass (charge) numbers A_L (Z_L) and A_H (Z_H) for the light (L) and heavy (H) fragments. Here, $A = A_L + A_H$ ($Z = Z_L + Z_H$) is the mass (charge) number of fissioning nucleus. By taking into consideration the volume conservation, the shape of the system is defined by the mass and charge numbers of the fragments, deformation parameters of fragments, β_i ($i = L,H$), and the interfragment distance R. The index i designates the light or heavy fragment of the DNS. The potential energy [6,9]

$$\begin{aligned} U(A_i,Z_i,\beta_i,R) = {} & U_L^{\mathrm{LD}}(A_L,Z_L,\beta_L) + \delta U_L^{\mathrm{shell}}(A_L,Z_L,\beta_L,E_H^*) \\ & + U_H^{\mathrm{LD}}(A_H,Z_H,\beta_H) \\ & + \delta U_H^{\mathrm{shell}}(A_H,Z_H,\beta_H,E_H^*) \\ & + V^C(A_i,Z_i,\beta_i,R) + V^N(A_i,Z_i,\beta_i,R) \end{aligned} \tag{1}$$

of the DNS consists of the energies of the fragments and energy $V^C + V^N$ of their interaction. The nuclei in the DNS have the excitation energies E_i^*. The energy of each fragment consists of the liquid-drop energy U_i^{LD} and deformation-dependent shell-correction term $\delta U_i^{\mathrm{shell}}$. The liquid-drop symmetry, Coulomb, and surface parts are calculated as

$$\begin{aligned} U_i^{\mathrm{sym}}(A_i,Z_i,E_i^*) = {} & 27.612\frac{(N_i - Z_i)^2}{A_i} \\ & \times [1 + 6 \times 10^{-4}E_i^*/A_i], \\ U_i^C(A_i,Z_i,\beta_i,E_i^*) = {} & \frac{3}{5}\frac{Z_i^2e^2}{R_{0i}}\frac{\beta_i^{1/3}}{\sqrt{\beta_i^2 - 1}} \\ & \times \ln[\beta_i + \sqrt{\beta_i^2 - 1}][1 - 0.12E_i^*/A_i], \\ U_i^{\mathrm{sur}}(A_i,Z_i,\beta_i,E_i^*) = {} & \sigma_i S_i[1 + 0.102E_i^*/A_i], \end{aligned} \tag{2}$$

with $R_{0i} = 1.2249A_i^{1/3}$ fm, the area S_i of nuclear surface, and the excitation-energy-dependent surface-tension coefficient $\sigma_i = \sigma_{0i}[1 + k_i(\beta_i - \beta_i^{\mathrm{g.s.}})^2]$, $\sigma_{0i} = 0.9517[1 - 1.7826(N_i - Z_i)^2/A_i^2]$, and

$$k_i = k_i(E_i^*) = \frac{\exp(-E_i^*/3.7)}{1 + \exp\{-0.063[C_{\mathrm{vib}}(Z_i,A_i) - 67]\}}.$$

Here, $\beta_i^{\mathrm{g.s.}}$ and $C_{\mathrm{vib}}(Z_i,A_i)$ are the ground-state deformation and the stiffness of the nucleus, respectively [6,9]. The excitation-energy dependence of the liquid-drop terms is taken in a similar form as in Ref. [22].

The shell-correction terms are calculated with the Strutinsky method and the two-center shell model [23]. The damping of the shell corrections with excitation energy E_i^* is introduced as

$$\begin{aligned} \delta U_i^{\mathrm{shell}}(A_i,Z_i,\beta_i,E_i^*) = {} & \delta U_i^{\mathrm{shell}}(A_i,Z_i,\beta_i,E_i^* = 0) \\ & \times \exp[-E_i^*/E_D], \end{aligned} \tag{3}$$

where $E_D = 18.5$ MeV is the damping constant. The interaction potential consists of the Coulomb interaction potential V^C of the two uniformly charged spheroids and the nuclear interaction potential [24]

$$V^N = \int \rho_L(\mathbf{r_1})\rho_H(\mathbf{R} - \mathbf{r_2})F(\mathbf{r_1} - \mathbf{r_2})d\mathbf{r_1}d\mathbf{r_2}, \tag{4}$$

in the form of the double folding of the Woods–Saxon nuclear densities ρ_i of the fragments and Skyrme-type density-dependent nucleon-nucleon interaction

$$F(\mathbf{r_1} - \mathbf{r_2}) = C_0\left[F_{\mathrm{in}}\frac{\rho_0(\mathbf{r_1})}{\rho_{00}} + F_{\mathrm{ex}}\left(1 - \frac{\rho_0(\mathbf{r_1})}{\rho_{00}}\right)\right]\delta(\mathbf{r_1} - \mathbf{r_2}),$$

where $\rho_0(\mathbf{r}) = \rho_L(\mathbf{r}) + \rho_H(\mathbf{R} - \mathbf{r})$,

$$F_{\mathrm{in}} = f_{\mathrm{in}} + f'_{\mathrm{in}}\frac{(N_L - Z_L)(N_H - Z_H)}{(N_L + Z_L)(N_H + Z_H)},$$

$$F_{\mathrm{ex}} = f_{\mathrm{ex}} + f'_{\mathrm{ex}}\frac{(N_L - Z_L)(N_H - Z_H)}{(N_L + Z_L)(N_H + Z_H)},$$

$C_0 = 300$ MeV fm^3, $f_{\mathrm{in}} = 0.09$, $f_{\mathrm{ex}} = -2.59$, $f'_{\mathrm{in}} = 0.42$, $f'_{\mathrm{ex}} = -0.54$, and $\rho_{00} = 0.17$ fm^{-3}. The nuclear densities are taken in the two-parameter Woods–Saxon form with the diffuseness parameter $a = 0.51$–0.56 fm depending on the charge number of the nucleus. The interaction potential has an inner pocket and external barrier located at the distances between the tips of the fragments of about (0.5–1) fm and (1.5–2) fm (in the considered region of fission fragments), respectively, depending on deformations of the fragments. The internuclear distance R in Eq. (1) corresponds to the position of this pocket (minimum) $R = R_m(A_i,Z_i,\beta_i)$. The quasifission barrier, $B_{qf}(A_i,Z_i,\beta_i)$, calculated as the difference of the potential energies between the bottom of the inner pocket [$R = R_m(A_i,Z_i,\beta_i)$] and the top of the external barrier [$R = R_b(A_i,Z_i,\beta_i)$], prevents the decay of the DNS in R [21]. Note that the height of quasifission barrier decreases with charge asymmetry.

Because the thermodynamic equilibrium is assumed at the scission point, the excitation energy $E^*(A_i,Z_i,\beta_i,R_m)$ at scission is calculated as the initial excitation energy of the fissioning nucleus $E_{CN}^* = E_n + Q$ (E_n is the neutron energy) plus the difference between the potential energies of the fissioning nucleus $U_{CN}(A,Z,\beta)$ and the system at the scission point $U(A_i,Z_i,\beta_i,R_m)$ [6]:

$$E^*(A_i,Z_i,\beta_i,R_m) = E^*_{CN} + [U_{CN}(A,Z,\beta) - U(A_i,Z_i,\beta_i,R_m)]. \tag{5}$$

The relative formation probability of the DNS with particular masses, charges, and deformations of the fragments is calculated with the statistical approach as follows [21]:

$$w(A_i,Z_i,\beta_i,E^*) = N_0 \exp\left[-\frac{U(A_i,Z_i,\beta_i,R_m)+B_{qf}(A_i,Z_i,\beta_i)}{T}\right], \tag{6}$$

where N_0 is the normalization factor. In Eq. (6) the temperature is calculated as $T = \sqrt{E^*/a}$, where $a = A/12$ MeV^{-1} is the level density parameter in the Fermi-gas model. In our calculations, a single value is used for the temperature calculated at the global minimum of U before the shell damping. As seen, the height $B_{\rm qf}$ of the quasifission barrier also has an impact on the yields. With increasing elongation and decreasing charge (mass) asymmetry the value of $B_{\rm qf}$ decreases, the system becomes more unstable and decays.

In order to obtain the mass distribution in fission of a particular nucleus with the mass number A_i and charge number Z_i, one should integrate Eq. (6) over β_L and β_H:

$$Y(A_i,Z_i,E^*) = N_0 \int d\beta_L d\beta_H w(A_i,Z_i,\beta_i,E^*). \tag{7}$$

All distributions are normalized to unity. Finally, for the calculations of mass and charge distributions the following expressions are obtained:

$$Y(A_i) = N_0 \sum_{Z_i} \int d\beta_L d\beta_H w(A_i,Z_i,\beta_i,E^*), \tag{8}$$

$$Y(Z_i) = N_0 \sum_{A_i} \int d\beta_L d\beta_H w(A_i,Z_i,\beta_i,E^*). \tag{9}$$

Because the dynamical treatment is not explicitly performed here, we "simulate" the dynamical effects by restricting the minimum value of the quasifission barrier. In the calculations, we take into consideration only those configurations for which $B_{\rm qf}$ is larger than 1 MeV. This condition restricts the highly deformed unstable configurations in the (β_L,β_H) plane and, correspondingly, restricts the upper limits of integration over deformations β_L and β_H. As shown below, this restriction allows us to describe the experimental data rather well.

Because of the excitation energy, the fission fragment can evaporate several neutrons after fission. This changes the mass distribution but not the charge distribution. To calculate the neutron multiplicity distribution, the following expression is used:

$$\langle n_i\rangle = \frac{E_i^{'*}}{B_{n_i} + 2T_i}. \tag{10}$$

Here, B_{n_i} and $2T_i$ are the separation energy and the kinetic energy of the evaporated neutron, respectively. Two nuclei share the total excitation energy proportional to their masses. Since the fragments are deformed at scission, the relaxation of the deformations to the ground-state values increases the excitation energy of the nucleus by an amount equal to the deformation energy $E_i^{\rm def}$. So,

$$E_i^{'*} = E^*\frac{A_i}{A_L+A_H} + E_i^{\rm def}. \tag{11}$$

In the calculations of mass distributions we included the postscission neutron evaporation.

The scission-point model is also suitable for describing the total kinetic energy (TKE) of the fission fragments. We calculate the TKE supposing that all interaction energy at the scission point transforms after fission into the kinetic energy of the fission fragments. Therefore, the value of the TKE strongly depends on the deformations of the fragments at the scission point. The smaller are the deformations of the fragments, the larger is the Coulomb repulsion, and the larger is the TKE. The mean value of the TKE for particular binary splitting is calculated by averaging over the deformations of the fragments:

$$\langle {\rm TKE}\rangle(A_i,Z_i) = \frac{\int {\rm TKE}(A_i,Z_i,\beta_i) w(A_i,Z_i,\beta_i,E^*) d\beta_L d\beta_H}{\int w(A_i,Z_i,\beta_i,E^*) d\beta_L d\beta_H}, \tag{12}$$

where

$${\rm TKE}(A_i,Z_i,\beta_i) = V^C(A_i,Z_i,\beta_i,R_b) + V^N(A_i,Z_i,\beta_i,R_b). \tag{13}$$

The mean TKE as a function of fragment mass A_i and charge Z_i are calculated as

$$\langle {\rm TKE}\rangle(A_i) = \frac{\sum_{Z_i} {\rm TKE}(A_i,Z_i) Y(A_i,Z_i,E^*)}{\sum_{Z_i} Y(A_i,Z_i,E^*)}, \tag{14}$$

$$\langle {\rm TKE}\rangle(Z_i) = \frac{\sum_{A_i} {\rm TKE}(A_i,Z_i) Y(A_i,Z_i,E^*)}{\sum_{A_i} Y(A_i,Z_i,E^*)}. \tag{15}$$

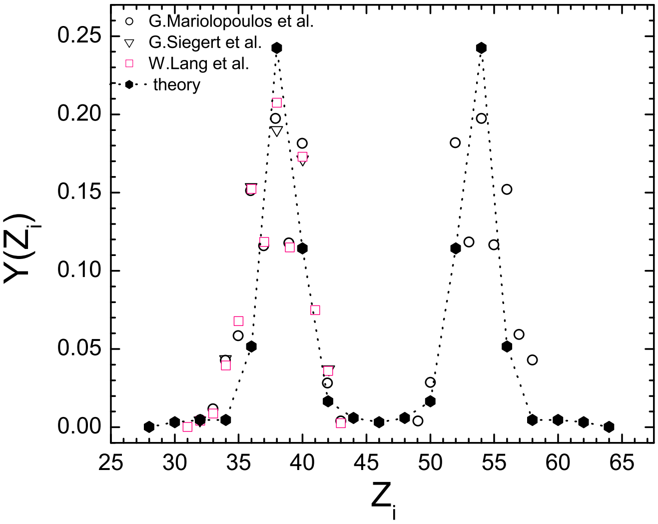

FIG. 1. The calculated charge distribution (solid circles connected by dotted lines to guide eye) for fission of ^{235}U by thermal neutron is compared with the experimental data (symbols) from Refs. [28–30]. The calculations were performed for even-Z_i fragments.

III. DISCUSSIONS OF CALCULATED RESULTS

We perform the calculations of the charge and mass distributions of the fragments in neutron-induced fission of nuclei ^{235,238}U and ^{239}Pu. As a first step, the calculations were restricted only to even-even fission fragments which mainly define the shapes of the charge and mass distributions. The inclusion of the odd-even and odd-odd fission fragments can elucidate even-odd effects but cannot appreciably change the smooth part of charge (mass) distributions in which we are interested. The even-odd effects would add some oscillations to this smooth part. To obtain a smoother curve for the mass distribution and to simulate the minimal experimental uncertainty in the measurement of the mass number of the fission fragment, each calculated yield is smeared by the Gaussian with the width $\sigma_{A_L} = 1.5$ amu. The calculations were corrected for the neutron evaporation from the fragments as described in Sec. II. We assume that the neutron emission prior to fission will not cause major change in the yield for the plutonium and uranium systems.

A. Fission reaction ^{235}U(n,f)

To test the model description, the calculated results are compared with the available experimental data. Our model provides a good description of the charge-yields in the fission reaction ^{235}U(n,f) with the thermal neutron (Fig. 1). In this reaction, the asymmetric charge (mass) distribution was observed. In Fig. 2 we also show the calculated charge distributions of fragments in the electromagnetic-induced fission reactions ^{230,232}U and ^{214,218}Ra and compare with the experimental data from Ref. [2]. The average excitation energy of these fissioning nuclei is about 11 MeV [2]. Our calculations of the mass yields [Fig. 3] reproduce the experimental data in the mass range $A_L = 100$–118. The mass yields for $A_L = 94$–100 are slightly overestimated, while the mass yields for $A_L < 94$ are underestimated. The latter discrepancies are unclear since we have a good description of the charge distribution in the corresponding mass region. One can assume that the wider experimental width in Fig. 3 is due to dynamical processes which are currently beyond the scope of the simplistic model

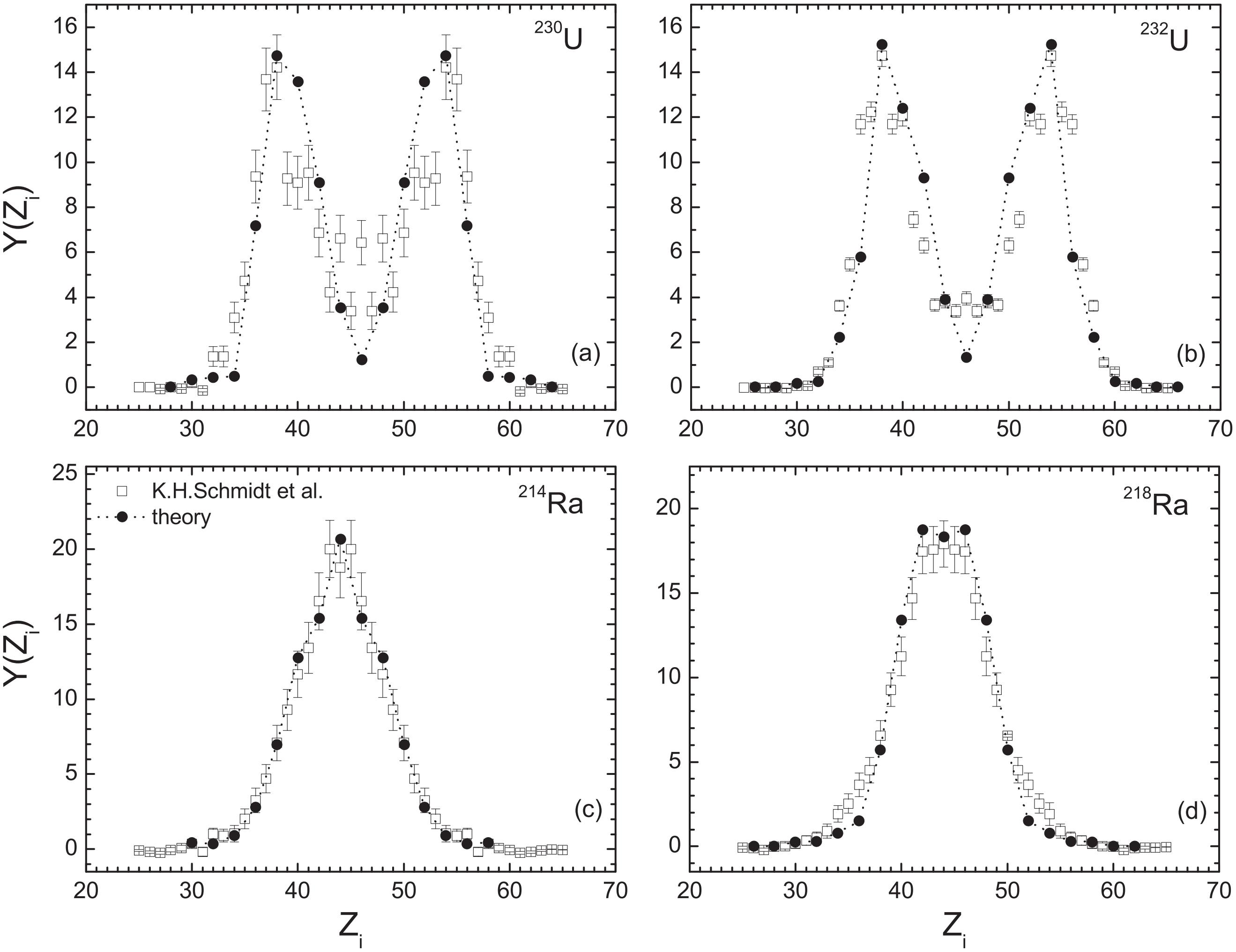

FIG. 2. The calculated charge distributions (solid circles connected by dotted lines to guide eye) in the electromagnetic-induced fission reactions (a) ^{230}U, (b) ^{232}U, (c) ^{214}Ra, and (d) ^{218}Ra are compared with the experimental data (symbols) from Ref. [2]. The average excitation energy of these fissioning nuclei is about of 11 MeV [2]. The calculations were performed for even-Z_i fragments.

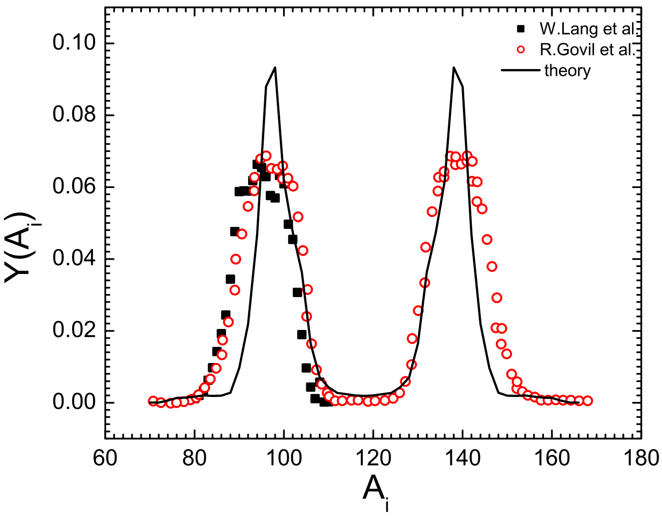

FIG. 3. The calculated mass distribution (solid line) for fission of ^{235}U by thermal neutron is compared with the experimental data (symbols) from Refs. [28,31].

presented here. However, in contrast to the calculated results for the thermal-neutron-induced fission, the mass distributions for 6 and 14 MeV neutron-induced fission of ^{235}U are well reproduced (Fig. 4). The influence of the excitation energy on the peak-to-valley ratio in the mass yields is well described

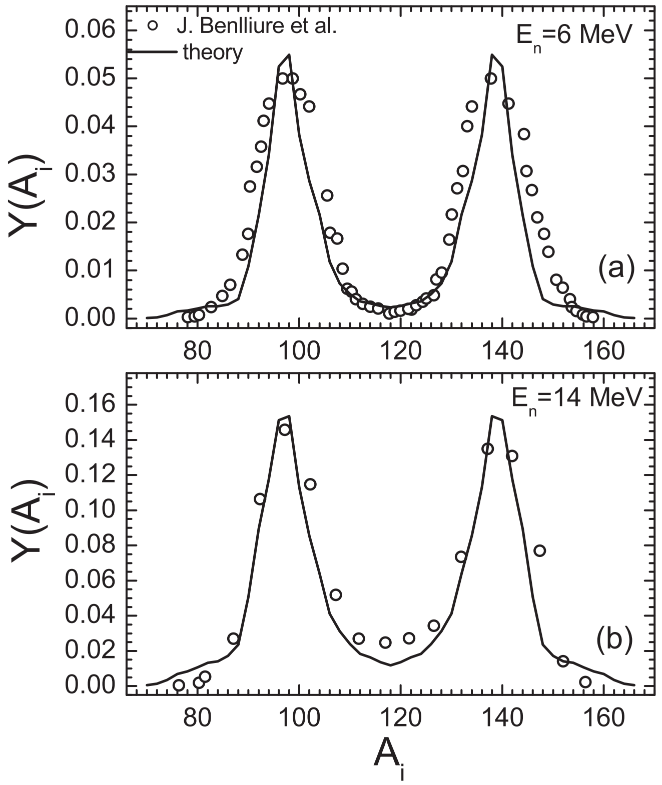

FIG. 4. The calculated mass distributions (solid lines) for fission of ^{235}U by neutron with incident energies (a) 6 MeV and (b) 14 MeV. The experimental data (symbols) are from Ref. [32].

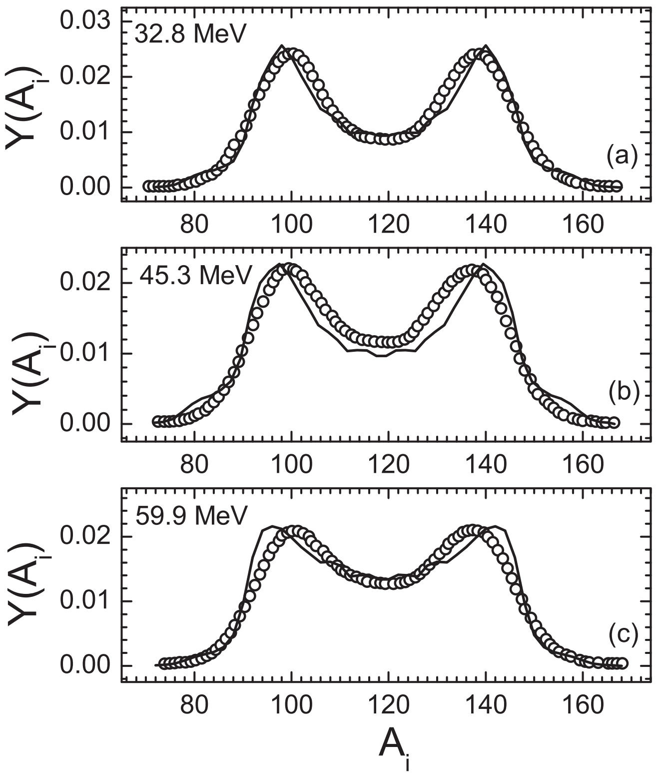

FIG. 5. The calculated fragment mass distribution (solid lines) is compared with the experimental data [15] for the ^{238}U(n,f) reaction at indicated incident neutron energies (a) 32.8, (b) 45.3, and (c) 59.9 MeV.

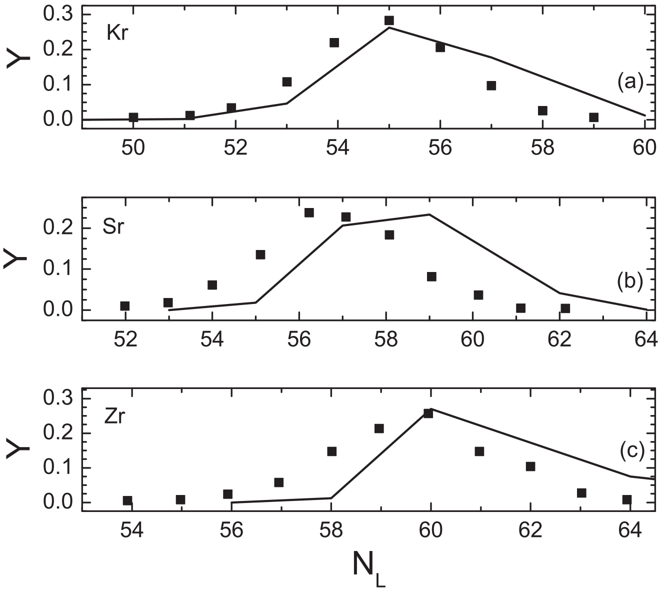

FIG. 6. The calculated mass yields (solid lines) of the (a) Kr, (b) Sr, and (c) Zr isotopes as a function of neutron number N_L in fission of ^{235}U by thermal neutrons. The neutron emissions from the primary fragments were taken into consideration. The experimental data (symbols) are from Ref. [28].

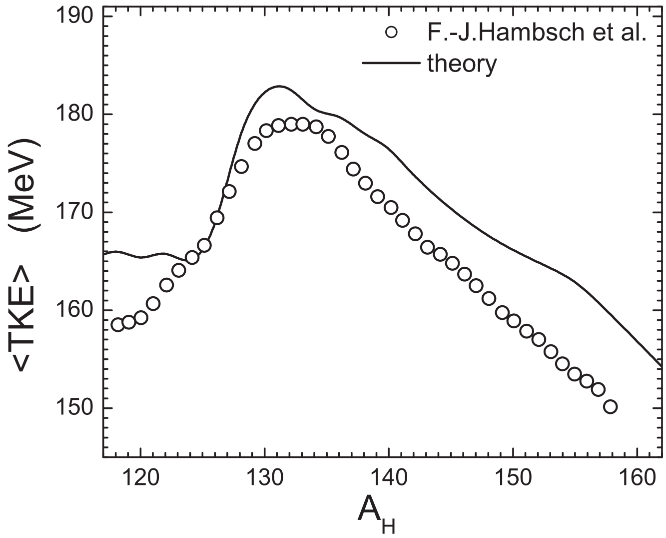

FIG. 7. The calculated (solid line) and experimental (symbols) [13] average total kinetic energies as functions of fragment mass in fission of ^{235}U by thermal neutrons.

within our model. Note that the peak-to-valley ratio in the mass yields is identical to that in the charge yields. In Fig. 5, the calculated mass distributions of the 32.8, 45.3, and 59.9 MeV neutron-induced fission of ^{238}U are also in a good agreement with the experimental data. In addition, the present model allows us to describe quite well the isotopic distributions of fission fragments in the ^{235}U(n_{th},f) reaction with thermal neutrons (Fig. 6).

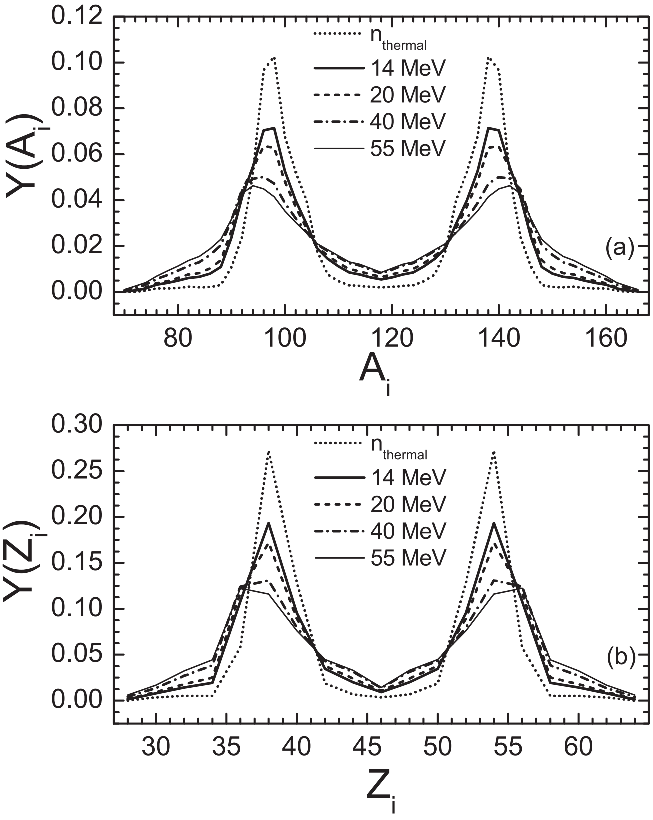

FIG. 8. (a) The calculated fragment mass and (b) charge distributions in the ^{235}U(n,f) reaction at the incident neutron energies indicated. The calculations were performed for even-Z_i fragments.

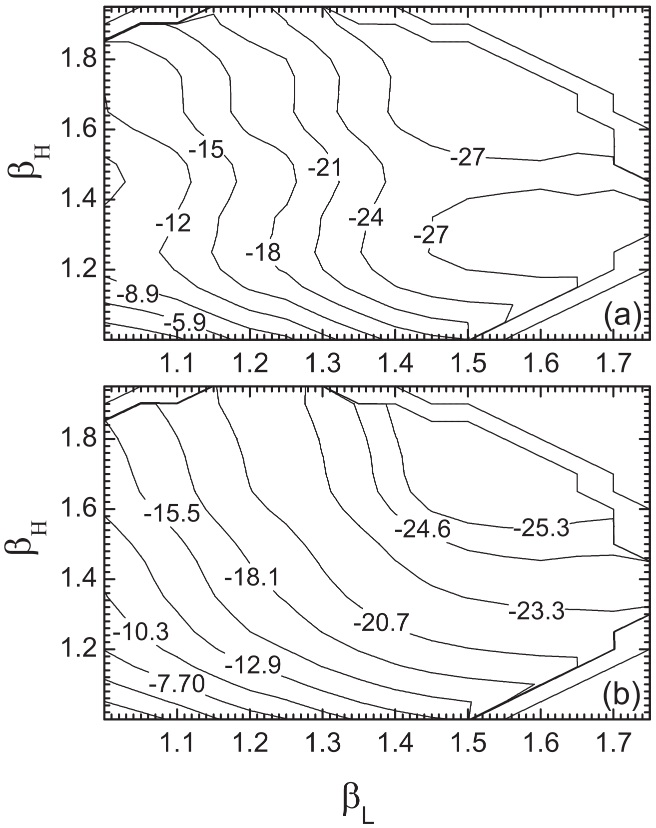

FIG. 9. The calculated potential-energy surfaces (in MeV) for the DNS with $(A_L,Z_L) = (96{,}36)$ and $(A_H,Z_H) = (140{,}56)$ at (a) $E_n = 0$ MeV and (b) $E_n = 55$ MeV. The value of potential energy is normalized to the energy of the DNS with the spherical nuclei ($\beta_L = \beta_H = 1$). In the nuclear shape parametrization used, the value of quadrupole deformation parameter is approximately $\beta_i - 1$ ($i = L,H$).

Figure 7 demonstrates the calculated dependence of ⟨TKE⟩ on A_H for the thermal neutron-induced fission of ^{235}U. The shape of this distribution is satisfactorily reproduced. The largest deviations between the theoretical and experimental results are observed for the very asymmetric ($A_H \geqslant 150$) and symmetric fission events. Because the dynamical effects are not included in the model presented, one can assume that these effects are important for the asymmetric fission. In Ref. [6] only a few mass splittings were considered for each charge splitting, while in the present paper more mass splittings were taken into account.

To study the influence of bombarding energy (excitation energy) on the shape of the fission-fragment mass, charge, and isotopic distributions, we consider the reactions ^{235}U(n,f) at incident neutron energies $E_n = 14$, 20, 40, and 55 MeV. With increasing E_n the mass yields (charge yields) clearly show the decrease of asymmetric peaks and an increase of fission yields in the near-symmetric mass (charge) region and asymmetric region with $A_L < 90$ ($Z_L < 36$) (Fig. 8). The ratio between

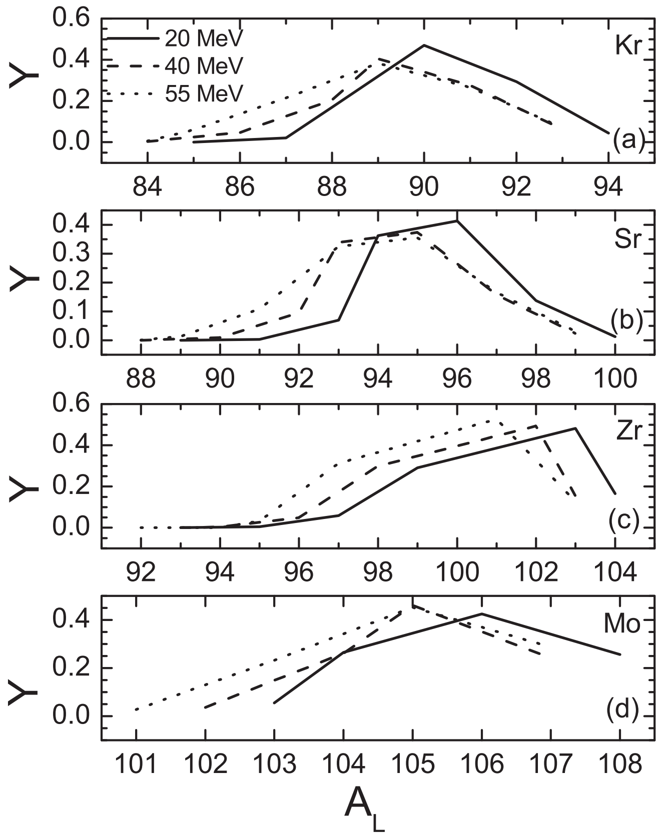

FIG. 10. The calculated isotopic trends for the nuclei (a) Kr, (b) Sr, (c) Zr, and (d) Mo in the ^{235}U(n,f) reaction at different indicated neutron energies.

the relative yields of the fragments with $A_L = 90$–100 and with $A_L = 110$–118 is reduced. The increase in the $A = 118$ region with neutron energy is also reported in the literature (see, for example, Ref. [4]). The yields of near-symmetric fission fragments increase nearly monotonically with incident energy from 14 to 55 MeV. Our results indicate that the combined energy-dependent structures on the potential-energy surface governs the yields of the fragments. The excitation energy reduces the shell effects that cause a widening of the minima in the deformation space and a migration of the minima in the potential-energy surface (Fig. 9). As a result, the mass and charge distributions are changed (Fig. 8). However, the influence of excitation energy is not so dramatic. The mass distribution has a pronounced asymmetric shape even at the incident neutron energy $E_n = 55$ MeV which needs the experimental verification.

As seen in Fig. 8, the charge distribution does not significantly change with increasing E_n. The variations of the charge-distribution with excitation energy cause a weak change of the Coulomb barrier value averaged over all charge splits at fixed mass asymmetry, which is accompanied by a correlated change of $\langle \mathrm{TKE} \rangle (A_H)$ within a few MeV with E_n. One can suggest the direct experimental verification of the weak energy dependence of the average TKE.

In Fig. 10, the isotopic trends of the fragments with $Z =$ 36, 38, 40, and 42 are predicted at various incident neutron energies. The only notable change in the yields with energy is the shift of position of the maximum towards lower mass (neutron) numbers. This is easily explained by the increase of neutron evaporation from the fragments with excitation energy.

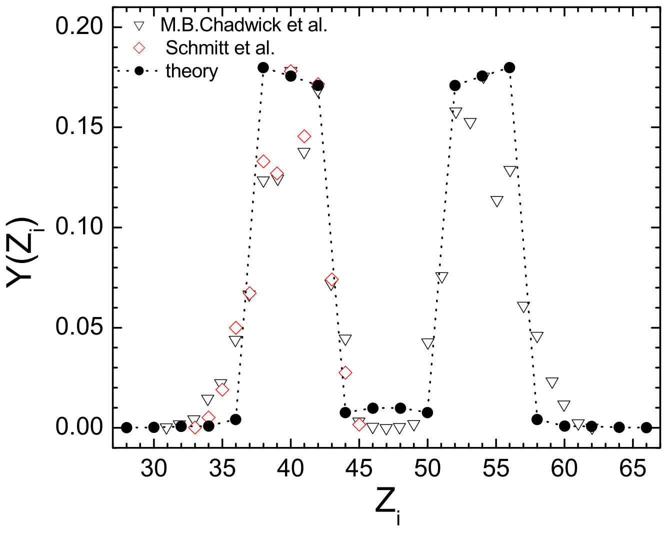

FIG. 11. The calculated (solid circles connected by dotted lines to guide eye) fragment charge distribution in the ^{239}Pu(n_{th},f) reaction is compared with the experimental data (symbols) from Refs. [25,26]. The calculations were performed for even-Z_i fragments.

B. Fission reaction ^{239}Pu(n,f)

In Figs. 11 and 12, the calculated charge and mass distributions are compared with the experimental data from

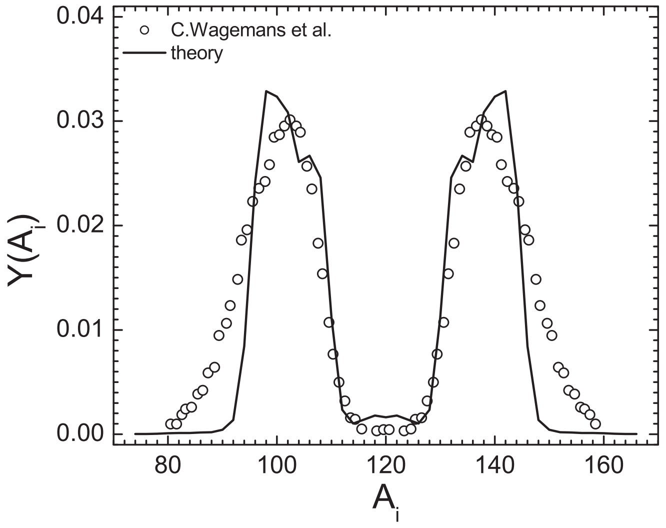

FIG. 12. The calculated (solid line) fragment mass distribution in the ^{239}Pu(n_{th},f) reaction is compared with the experimental data (symbols) from Ref. [27].

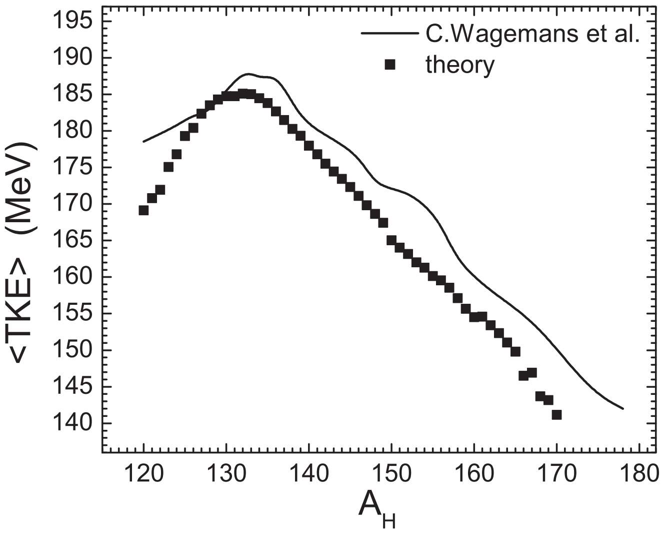

FIG. 13. The calculated (solid line) average total kinetic energies of fission fragments in the ^{239}Pu(n_{th},f) reaction versus fragment mass. The experimental data (symbols) are from Ref. [27].

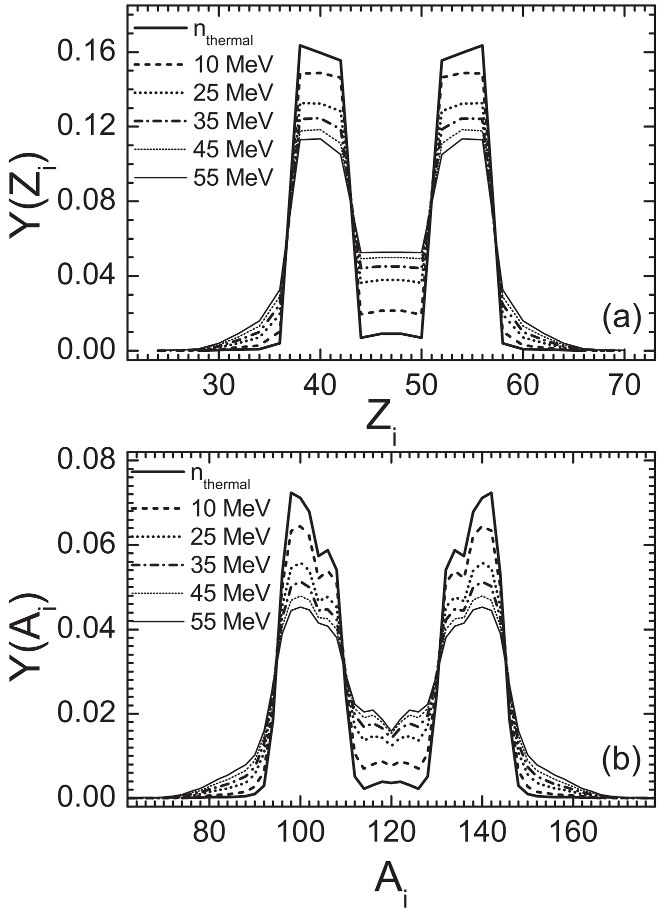

FIG. 14. The (a) charge and (b) mass distributions predicted for the ^{239}Pu(n,f) reaction at different indicated neutron energies. The calculations were performed for even-Z_i fragments.

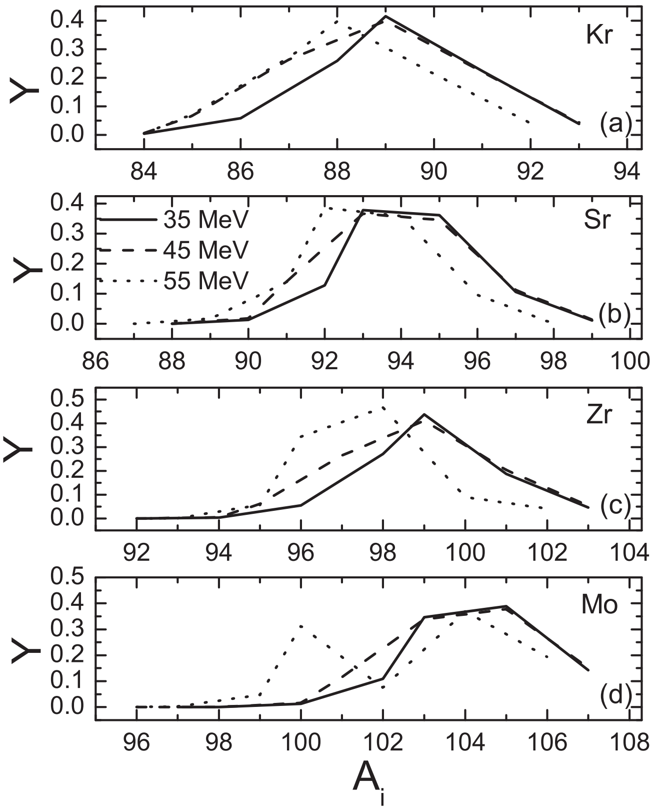

FIG. 15. The predicted isotopic trends for (a) the nuclei Kr, (b) Sr, (c) Zr, and (d) Mo in the ^{239}Pu(n,f) reaction at indicated neutron energies.

Refs. [25–27], respectively, for the ^{239}Pu(n,f) reaction at the thermal-neutron energy. A good agreement with the experimental data is obtained. The central peak recedes. The quality of description of the mass (charge) distribution is the same as in the ^{235}U case. For the thermal-neutron-induced fission of ^{239}Pu, the evolution of the average total kinetic energy with fragment mass number is shown in Fig. 13. As in the case of the neutron-induced fission of ^{235}U, a small change of $\langle$TKE$\rangle$ with increasing excitation energy is predicted. In Figs. 14, and 15, the mass and charge, and isotopic distributions are predicted at the energies $E_n = 10$, 25, 35, 45, and 55 MeV of the incident neutron. The changes of the shapes of distributions are similar to the ^{236}U and have the same explanation. Note that the mass and charge distributions remain asymmetric even at high excitation energies of the fissioning nucleus, about 60 MeV.

IV. CONCLUSIONS

The improved scission-point statistical model was employed to describe the fission reactions with actinides. The key element of the model is the calculation of the potential-energy surfaces. Knowledge of the deformations of the nascent DNS at the moment of scission is crucial. The simple restriction of maximum deformations of the DNS nuclei proposed in this paper tries to mimic some dynamical effects while still retaining all the features of the statistical model. We provided a good description of the charge and mass distributions, isotopic trends, and the total kinetic energy of the fission fragments in the reactions $^{235}\mathrm{U}+n$ and $^{239}\mathrm{Pu}+n$. For these reactions, the influence of the excitation energy on the mass, charge, and isotopic distributions as well as the average total kinetic energies of fission fragments for higher neutron energies, up to 55 MeV, was studied. The evolution of these fission characteristics with increasing energy was shown to be related with the widening and migration of the minima in the potential-energy surface. The important result was the conservation of the asymmetric shapes of the mass and charge distributions of the fission fragments at sufficiently high excitation energies of the fissioning nucleus. One can hope that presented predictions of the energy dependence of the fission observables will encourage future experiments to explore neutron-induced fission at higher bombarding energies. The detailed comparisons between our predictions and new experimental data are expected to add to our understanding of the fission process. The present model can be also employed for the description of electromagnetic-, charged-particle-, and nucleon-transfer-induced fission at high excitation energies of a compound nucleus.

ACKNOWLEDGMENTS

This work was partially supported by RFBR and Romania-JINR Cooperation program.

---

[1] A. N. Andreyev, M. Huyse, and P. Van Duppen, Rev. Mod. Phys. **85**, 1541 (2013).

[2] K.-H. Schmidt *et al.*, Nucl. Phys. A **665**, 221 (2000); **693**, 169 (2001).

[3] A. N. Andreyev, J. Elseviers, M. Huyse, P. VanDuppen, S. Antalic, A. Barzakh, N. Bree, T. E. Cocolios, V. F. Comas, J. Diriken, D. Fedorov, V. Fedosseev, S. Franchoo, J. A. Heredia, O. Ivanov, U. Koster, B. A. Marsh, K. Nishio, R. D. Page, N. Patronis, M. Seliverstov, I. Tsekhanovich, P. VandenBergh, J. VanDeWalle, M. Venhart, S. Vermote, M. Veselsky, C. Wagemans, T. Ichikawa, A. Iwamoto, P. Moller, and A. J. Sierk, Phys. Rev. Lett. **105**, 252502 (2010).

[4] U. Brosa, S. Grossmann, and A. Müller, Phys. Rep. **197**, 167 (1990).

[5] B. D. Wilkins, E. P. Steinberg, and R. R. Chasman, Phys. Rev. C **14**, 1832 (1976).

[6] A. V. Andreev, G. G. Adamian, N. V. Antonenko, S. P. Ivanova, and W. Scheid, Eur. Phys. J. A **22**, 51 (2004); **26**, 327 (2005).

[7] M. Warda, A. Staszczak, and W. Nazarewicz, Phys. Rev. C **86**, 024601 (2012).

[8] S. Panebianco, J.-L. Sida, H. Goutte, J.-F. Lemaître, N. Dubray, and S. Hilaire, Phys. Rev. C **86**, 064601 (2012).

[9] A. V. Andreev, G. G. Adamian, and N. V. Antonenko, Phys. Rev. C **86**, 044315 (2012); **88**, 047604 (2013).

[10] M. Caamaño, F. Farget, O. Delaune, K. H. Schmidt, C. Schmitt, L. Audouin, C. O. Bacri, J. Benlliure, E. Casarejos, X. Derkx, B. Fernandez-Dominguez, L. Gaudefroy, C. Golabek, B. Jurado, A. Lemasson, D. Ramos, C. Rodriguez-Tajes, T. Roger, and A. Shrivastava, Phys. Rev. C **92**, 034606 (2015).

[11] J. Randrup and P. Möller, Phys. Rev. Lett. **106**, 132503 (2011); Phys. Rev. C **84**, 034613 (2011); P. Möller, J. Randrup, and A. J. Sierk, *ibid.* **85**, 024306 (2012).

[12] L. E. Glendenin, J. E. Gindler, D. J. Henderson, and J. W. Meadows, Phys. Rev. C **24**, 2600 (1981).

[13] Ch. Straede, C. Budtz-Jorgensen, and H.-H. Knitter, Nucl. Phys. A **462**, 85 (1987); F.-J. Hambsch, H.-H. Knitter, and C. Budtz-Jorgensen, *ibid.* **491**, 56 (1989).

[14] M. C. Duijvestijn, A. J. Koning, and F.-J. Hambsch, Phys. Rev. C **64**, 014607 (2001).

[15] I. V. Ryzhov, S. G. Yavshits, G. A. Tutin, N. V. Kovalev, A. V. Saulski, N. A. Kudryashev, M. S. Onegin, L. A. Vaishnene, Y. A. Gavrikov, O. T. Grudzevich, V. D. Simutkin, S. Pomp, J. Blomgren, M. Osterlund, P. Andersson, R. Bevilacqua, J. P. Meulders, and R. Prieels, Phys. Rev. C **83**, 054603 (2011).

[16] H. Naik, S. Mukerji, R. Crasta, S. V. Suryanarayana, S. C. Sharma, and A. Goswani, Nucl. Phys. A **941**, 16 (2015).

[17] A. Deppman, E. Andrade-II, V. Guimarães, G. S. Karapetyan, and N. A. Demekhina, Phys. Rev. C **87**, 054604 (2013); A. Deppman, E. Andrade-II, V. Guimarães, G. S. Karapetyan, A. R. Balabekyan, and N. A. Demekhina, *ibid.* **88**, 024608 (2013); A. Deppman, E. Andrade-II, V. Guimaraes, G. S. Karapetyan, O. A. P. Tavares, A. R. Balabekyan, N. A. Demekhina, J. Adam, F. Garcia, and K. Katovsky, *ibid.* **88**, 064609 (2013).

[18] M. Caamaño, O. Delaune, F. Farget, X. Derkx, K. H. Schmidt, L. Audouin, C. O. Bacri, G. Barreau, J. Benlliure, E. Casarejos, A. Chbihi, B. Fernandez-Dominguez, L. Gaudefroy, C. Golabek, B. Jurado, A. Lemasson, A. Navin, M. Rejmund, T. Roger, A. Shrivastava, and C. Schmitt, Phys. Rev. C **88**, 024605 (2013).

[19] H. Naik, A. Goswani, G. N. Kim, K. Kim, and S. V. Suryanarayana, Eur. Phys. J. A **49**, 133 (2013).

[20] J. L. Rodríguez-Sánchez *et al.*, Phys. Rev. C **91**, 064616 (2015).

[21] Sh. A. Kalandarov, G. G. Adamian, N. V. Antonenko, and W. Scheid, Phys. Rev. C **82**, 044603 (2010); **83**, 054611 (2011); Sh. A. Kalandarov, G. G. Adamian, N. V. Antonenko, W. Scheid, and J. P. Wieleczko, *ibid.* **84**, 064601 (2011).

[22] G. Sauer, H. Chandra, and U. Mosel, Nucl. Phys. A **264**, 221 (1976).

[23] J. Maruhn and W. Greiner, Eur. Phys. J. A **251**, 431 (1972).

[24] G. G. Adamian *et al.*, Int. J. Mod. Phys. E **05**, 191 (1996).

[25] C. Schmitt *et al.*, Nucl. Phys. A **430**, 21 (1984).

[26] M. B. Chadwick *et al.*, Nucl. Data Sheets **107**, 2931 (2006).

[27] C. Wagemans, E. Allaert, A. Deruytter, R. Barthelemy, and P. Schillebeeckx, Phys. Rev. C **30**, 218 (1984).

[28] W. Lang, H. G. Clerc, W. Wohlfarth, H. Schrader, and K.-H. Schmidt, Nucl. Phys. A **345**, 34 (1980).

[29] G. Siegert, H. Wollnik, J. Grief, R. Decker, G. Fiedler, and B. Pfeiffer, Phys. Rev. C **14**, 1864 (1976).

[30] G. Mariolopoulos, Ch. Hamelin, J. Blachot, J. P. Boucqet, B. Brissot, J. Crancon, H. Nifenecker, and Ch. Ristori, Nucl. Phys. A **361**, 213 (1981).

[31] R. Govil, S. S. Kapoor, D. M. Nadkarni, S. R. S. Murthy, and P. N. Rama Rao, Nucl. Phys. A **410**, 458 (1983).

[32] J. Benlliure *et al.*, Nucl. Phys. A **628**, 458 (1998).